

An Investigation of the Presence of Atmospheric Rivers over the North Pacific during Planetary-Scale Wave Life Cycles and Their Role in Arctic Warming

CORY BAGGETT, SUKYOUNG LEE, AND STEVEN FELDSTEIN

Department of Meteorology, The Pennsylvania State University, University Park, Pennsylvania

(Manuscript received 20 January 2016, in final form 8 July 2016)

ABSTRACT

Heretofore, the tropically excited Arctic warming (TEAM) mechanism put forward that localized tropical convection amplifies planetary-scale waves, which transport sensible and latent heat into the Arctic, leading to an enhancement of downward infrared radiation and Arctic surface warming. In this study, an investigation is made into the previously unexplored contribution of the synoptic-scale waves and their attendant atmospheric rivers to the TEAM mechanism. Reanalysis data are used to conduct a suite of observational analyses, trajectory calculations, and idealized model simulations. It is shown that localized tropical convection over the Maritime Continent precedes the peak of the planetary-scale wave life cycle by ~10–14 days. The Rossby wave source induced by the tropical convection excites a Rossby wave train over the North Pacific that amplifies the climatological December–March stationary waves. These amplified planetary-scale waves are baroclinic and transport sensible and latent heat poleward. During the planetary-scale wave life cycle, synoptic-scale waves are diverted northward over the central North Pacific. The warm conveyor belts associated with the synoptic-scale waves channel moisture from the subtropics into atmospheric rivers that ascend as they move poleward and penetrate into the Arctic near the Bering Strait. At this time, the synoptic-scale waves undergo cyclonic Rossby wave breaking, which further amplifies the planetary-scale waves. The planetary-scale wave life cycle ceases as ridging over Alaska retrogrades westward. The ridging blocks additional moisture transport into the Arctic. However, sensible and latent heat amounts remain elevated over the Arctic, which enhances downward infrared radiation and maintains warm surface temperatures.

1. Introduction

In our current climate, the Arctic is experiencing warming proportionally greater than other regions of Earth, a phenomenon known as Arctic amplification (Serreze and Barry 2011). The consequences of a warming Arctic and its melting sea ice are geopolitical, biological, and meteorological—such as the opening of shipping lanes and oil fields to exploration; the disruption of the habitats and ecosystems of native species; and a higher frequency of atmospheric blocking and cold-air outbreaks during winter in the midlatitudes (Honda et al. 2009; Overland and Wang 2010; Francis and Vavrus 2012; Liu et al. 2012). Many various mechanisms, ranging from atmospheric to oceanic to local thermodynamic feedbacks, have been proposed to

explain the Arctic amplification that is currently being observed and predicted by global climate models (Farrell 1990; Barron et al. 1993; Cai 2006; Langen and Alexeev 2007; Winton 2006; Striver and Huber 2007; Abbot and Tziperman 2008; Kump and Pollard 2008; Walsh et al. 2008).

Apart from the above processes, an additional atmospheric pathway that can produce Arctic amplification has been proposed recently. The tropically excited Arctic warming (TEAM) mechanism hypothesizes that localized tropical convection near the Maritime Continent can amplify planetary-scale wave (PSW) activity, which leads to enhanced poleward sensible and latent heat transports into the Arctic. As a result of these transports, downward infrared radiation (IR) increases, and Arctic surface warming ensues (Doyle et al. 2011; Lee et al. 2011a,b; Yoo et al. 2011, 2012a,b; Lee 2012; Kapsch et al. 2013; Ding et al. 2014; Flournoy et al. 2016). It is important to note that the poleward sensible and latent heat fluxes that occur when the TEAM mechanism operates act independently of the flux–gradient relationship of synoptic-scale baroclinic

Corresponding author address: Cory Baggett, Department of Meteorology, The Pennsylvania State University, 503 Walker Building, University Park, PA 16802.
E-mail: cfb128@psu.edu

waves (Lee 2014; Lee and Yoo 2014; Baggett and Lee 2015, hereafter BL15). In particular, BL15 identified through composite analysis the existence of a PSW life cycle (waves with zonal wavenumber $k = 1-3$) that amplifies and decays over a period of $\sim 1-2$ weeks and manifests ~ 10 days after enhanced convection over the Maritime Continent. This PSW life cycle is preceded by an equator-to-pole temperature gradient that is very close to its climatological value yet is followed by Arctic warming of significant amplitude and duration. Moreover, BL15 found no evidence of enhanced, or amplified, synoptic-scale wave (SSW; $k \geq 4$) activity during the PSW life cycle. These characteristics of the PSW life cycle make the TEAM mechanism a viable process for Arctic amplification. However, the mechanism's independence from enhanced SSW activity does not preclude the possibility that the propagation of SSWs is altered, or redirected poleward, via the influence of the meridionally amplified planetary-scale flow present during the PSW life cycle—a possibility we plan to explore in this study.

Recently, Woods et al. (2013) and Liu and Barnes (2015) investigated extreme moisture intrusions into the Arctic and their contributions to Arctic amplification. Reminiscent of the TEAM mechanism, they found that these intrusions are accompanied by planetary-scale, low-frequency atmospheric patterns [or “blocks” (e.g., Henderson et al. 2016)] that can divert moisture fluxes northward into the Arctic and thereby enhance downward IR and surface warming. They showed that these intrusions are intimately connected to SSW activity and Rossby wave breaking, have a filamentary structure, and rapidly convey moisture poleward, bearing a pronounced resemblance to atmospheric rivers (ARs; Newell et al. 1992; Zhu and Newell 1998; Neiman et al. 2008; Ralph et al. 2004; Ralph and Dettinger 2011; Newman et al. 2012; Krichak et al. 2015; Neff et al. 2014).

Although a myriad of definitions for ARs exist, they are generally characterized by having large values of total column water ($>20 \text{ kg m}^{-2}$), being longer ($>2000 \text{ km}$) than they are wide ($<1000 \text{ km}$), transporting moisture poleward rapidly, and being readily identifiable with satellite imagery. Underscoring the importance of ARs to the global water cycle and climate, Zhu and Newell (1998) found that ARs account for a substantial majority of the total poleward moisture transport in the midlatitudes, a result supported by more recent studies (e.g., Guan and Waliser 2015). Also, ARs contribute to extreme precipitation events across the world (Moore et al. 2012; Krichak et al. 2015; De Vries et al. 2016) and have been extensively studied for their impacts along the west coast of North America (Higgins et al. 2000; Roberge et al. 2009; Smith et al. 2010; Neiman et al. 2011). Newman et al.

(2012) expounded a more complex view of ARs, finding that the moisture transport by individual events consists of mean, low-frequency, and synoptic-scale contributions. For example, they suggest that low-frequency tropical forcing over the equatorial Pacific can produce an anomalous Aleutian low that contributes to the poleward moisture transport by ARs during high-frequency synoptic-scale events. Using the algorithm created by Zhu and Newell (1998) to identify ARs [described in section 2a(3)], this study plans to explore the characteristics of ARs entering the Arctic during the PSW life cycle.

Having identified the ARs that enter the Arctic, we also aim to identify their moisture source regions. Similar to prior studies that have investigated the moisture source regions of extreme precipitation events associated with midlatitude ARs (Bao et al. 2006; Roberge et al. 2009; Moore et al. 2012; Krichak et al. 2015; De Vries et al. 2016), we will employ Lagrangian backward trajectory analysis to reveal the moisture source regions of ARs entering the Arctic. The results of these prior analyses showed that the majority of midlatitude ARs have moisture source regions over the subtropical and extratropical oceanic basins as midlatitude troughs move equatorward (Kiladis and Feldstein 1994; Ralph et al. 2011) and converge moisture along their trailing cold fronts. However, source regions along the northern edge of the tropics could not be ruled out (Bao et al. 2006; Knippertz 2007; Knippertz and Wernli 2010; Knippertz et al. 2013). Trajectory analysis also revealed the close association of ARs to the warm conveyor belts (Carlson 1980) of synoptic-scale cyclones (Eckhardt et al. 2004). In fact, Bao et al. (2006) proposed that ARs be renamed as “moisture conveyor belts.” More recently, Dacre et al. (2015) attributed the moisture found in ARs to local evaporation and convergence within the warm sectors of cyclones rather than long-range transport.

Given the previously described results, we ask the following questions. First, do SSWs and their attendant ARs contribute to the poleward transport of moisture into the Arctic during the PSW life cycle? Second, does trajectory analysis reveal that the tropics serve as a possible source region of moisture for the ARs? Third, using an idealized model perturbed by tropical convective heating, can we reproduce the observed PSW life cycle? Finally, how do the results of the preceding questions modify our understanding of the TEAM mechanism? We note here that we constrain much of our analysis to the North Pacific while recognizing ARs play an important role over the North Atlantic as well (Woods et al. 2013; Liu and Barnes 2015). However, the PSW life cycle we identify develops in response to localized tropical convection over the Maritime Continent (Yoo et al. 2012a; BL15), and therefore the Rossby wave

response will be most notably present in the North Pacific (Sardeshmukh and Hoskins 1988).

We divide this study into two main components: an observational analysis of reanalysis data and an initial-value calculation using the dynamical core of a general circulation model. Section 2 describes the data and methods used for the observational analysis and the model calculations, while sections 3 and 4 describe their respective results. Section 5 concludes the paper with a summary schematic of the PSW life cycle.

2. Data and methods

a. Observational analysis

1) DATA

For the observational component of this study, we use daily 0000 UTC data spanning from 1979 to 2014 obtained from the European Centre for Medium-Range Weather Forecasts (ECMWF) interim reanalysis (ERA-Interim) project (Dee et al. 2011; ECMWF 2009). We acquire the following data: zonal wind u , meridional wind v , specific humidity q , mean sea level pressure (MSLP), total column water (TCW), vertically integrated eastward water vapor flux Q_λ , vertically integrated northward water vapor flux Q_ϕ , convective precipitation P_{conv} , and potential temperature θ on the 2 potential vorticity unit (PVU; 1 PVU = 10^{-6} K kg $^{-1}$ m 2 s $^{-1}$) surface $\theta_{2\text{PVU}}$. All of the data have a horizontal resolution of $2.5^\circ \times 2.5^\circ$, while u , v , and q have an additional dimension in the vertical consisting of 23 pressure levels.

2) SELECTION CRITERIA FOR PSW EVENTS

To identify events when the PSWs are amplified, we integrate over the Northern Hemisphere daily values of eddy kinetic energy (EKE) associated with $k = 1-3$. This integration may be formulated as

$$\text{EKE} = \frac{1}{2} \int (u_p^2 + v_p^2) dm.$$

Here, u_p and v_p represent the sum of the contributions of the PSWs to u and v , respectively, found via Fourier analysis in the longitudinal direction, and dm is an element of atmospheric mass. Because the integrations are performed daily, growth and decay of EKE on weekly time scales may be used to infer PSW life cycle events (BL15). To identify these events, we calculate anomalous daily values of EKE by subtracting the calendar-day climatology of EKE, which has had its high-frequency variability removed by retaining only the first two harmonics of its raw annual cycle. We first choose days whose anomalous daily value of EKE is greater than one

standard deviation [calculated using December–March (DJFM) daily values of EKE]. This yields 673 days, many of which are adjacent in time to each other. Because we are interested in identifying individual PSW life cycle events, we next isolate the days with the greatest values of EKE compared to the 14 calendar days both preceding and following it. This results in no two days chosen that lie within 14 days of each other and nets 102 PSW events. We perform composite analyses on all 102 events and only the top one-third (34 events) and find both analyses to be statistically significant and qualitatively the same. Because the composite analysis of the 34 events yields clearer results with larger magnitudes, we choose to present it. Finally, we note that daily anomalies of other variables presented in the observational analysis follow the same procedures used to find anomalous EKE.

3) DEFINITION OF \mathbf{Q}_r

During these PSW events, we diagnose the location and direction of flow of the ARs by first objectively identifying regions of intense moisture transport. We adopt the mathematical definition of an AR proposed by Zhu and Newell (1998) to achieve this goal. First, the horizontal moisture flux field $\mathbf{Q}_t = Q_\lambda \mathbf{i} + Q_\phi \mathbf{j}$ is partitioned into the sum of two fields $\mathbf{Q}_t = \mathbf{Q}_r + \mathbf{Q}_b$, where \mathbf{Q}_r is associated with the fluxes by ARs and \mathbf{Q}_b is associated with the broad background fluxes. To construct \mathbf{Q}_r , the magnitude of the total water vapor flux Q_t at each grid point is tested such that

$$\mathbf{Q}_r = \begin{cases} \mathbf{Q}_t & \text{if } Q_t \geq \bar{Q} + 0.3(Q_{\text{max}} - \bar{Q}) \\ 0 & \text{if } Q_t < \bar{Q} + 0.3(Q_{\text{max}} - \bar{Q}) \end{cases}. \quad (1)$$

Here, \bar{Q} and Q_{max} are respectively the zonal mean and max value of Q_t along a given latitude circle. The constant 0.3 is used to determine the strength of the rivers that compose \mathbf{Q}_r . Zhu and Newell (1998) tested a range of constants from 0.1 to 0.5 and found that 0.3 gave the most reasonable separation between \mathbf{Q}_r and \mathbf{Q}_b based on the cases they tested. In our study, we seek to develop a qualitative picture of the location and direction of flow of the ARs during the PSW life cycle rather than compute their total poleward moisture transport. To that end, we find that gently varying the constant does not have a discernible impact on our results. In fact, despite the somewhat arbitrary nature of the constant employed in Eq. (1), we find our results to be entirely consistent with recent studies that developed detection algorithms that incorporate both integrated water vapor transport and shape criteria to examine the anomalous frequency of occurrence of ARs as a function of tropical convection (Guan and

Waliser 2015; Mundhenk et al. 2016). Finally, we use a subsample of ERA-Interim data with 0.75° horizontal resolution to calculate Eq. (1) and find no discernible difference in our results—consistent with the sensitivity tests performed by Guan and Waliser (2015). Therefore, for the sake of computational efficiency, we use the 2.5° horizontal resolution throughout this study.

4) BACKWARD TRAJECTORY ANALYSIS VIA HYSPLIT

To determine the source regions of the ARs entering the Arctic, we perform backward trajectory calculations with the Hybrid Single-Particle Lagrangian Integrated Trajectory (HYSPLIT; Draxler and Rolph 2015) system of the National Oceanic and Atmospheric Administration (NOAA) Air Resources Laboratory (ARL). The HYSPLIT system calculates the advection of parcels using the three-dimensional wind field (u , v , and ω), which is interpolated both in time and space along the trajectory. To perform the trajectory analysis, we employ ERA-Interim data that we format for use in the HYSPLIT system. The formatted data have a horizontal resolution of 2.5° by 2.5° , a vertical resolution of 23 pressure levels (fully resolved between the surface and 500 hPa), and a time resolution of 6 h. We initialize HYSPLIT during the peak intensity of the ARs and perform backward trajectories on the parcels to determine their source regions. Furthermore, we track the following meteorological variables along each parcel's trajectory: pressure p , potential temperature θ , equivalent potential temperature θ_E , relative humidity, surface precipitation rate, and surface evaporation rate. HYSPLIT provides as direct output p , θ , and relative humidity. We acquire surface evaporation and precipitation rates from ERA-Interim and interpolate to the parcels' positions in time and space along their trajectories. We calculate θ_E according to Eq. (39) of Bolton (1980), allowing the latent heat of vaporization to vary as a function of air temperature. As a sensitivity test, we also perform the trajectory analysis using the National Centers for Environmental Prediction (NCEP)–National Center for Atmospheric Research (NCAR) reanalysis project (NNRP; Kalnay et al. 1996) data, which HYSPLIT is configured to run with by default. We find the qualitative nature of our results to be unchanged.

To choose the ARs during PSW events on which we perform backward trajectories, we examine individually the 34 PSW events and pick the AR with the highest value of Q_r (the magnitude of \mathbf{Q}_r) at 65°N between 130° and 250°E during lag days from -7 through $+7$ for each event. This results in 32 ARs, as two of the PSW events have no Q_r within the aforementioned ranges. The latitude of 65°N is chosen because Woods et al. (2013) and Liu and Barnes

(2015) chose 70° and 60°N , respectively, to identify extreme moisture intrusions into the Arctic. The range of longitudes captures the North Pacific sector. Having identified the horizontal position and time to start each of the 32 backward trajectories, we choose a range of starting elevations between 100 and 10 000 m. Since our aim is to determine if the intruding moisture has a tropical source region, and knowing that parcels tend to rise along isentropic surfaces, it is expected that higher, midtropospheric elevations are more likely to reveal tropical source regions. Indeed, we find that parcels starting at lower starting elevations tend to intersect the surface quickly along their backward trajectories, thereby revealing sources of moisture at higher latitudes (Roberge et al. 2009).

b. Model calculations

To explore the importance of tropical convection in both exciting the PSW life cycle and inducing poleward moisture transport, we employ the spectral dynamical core model from the NOAA Geophysical Fluid Dynamics Laboratory (GFDL). Our model is run for 28 days with a horizontal resolution of triangular 42 and a vertical resolution of 28 sigma σ levels. The model incorporates fourth-order horizontal diffusion with a damping time scale of 0.1 days at its smallest scale. Vertical diffusion is not included, but we find our results are insensitive to its absence. The model incorporates Newtonian cooling and Rayleigh friction, which are precisely formulated and parameterized according to Held and Suarez (1994).

The initial background fields for our model calculations correspond to the climatological DJFM values of u , v , p_s , q , and temperature T . Each field is derived from the monthly means of daily means of ERA-Interim data spanning from 1979 to 2014. Since the GFDL spectral dynamical core is a dry model, q is utilized only as a passive tracer q_{tr} in order to study the influence of the model's evolving flow field on the redistribution of atmospheric water vapor. Therefore, q_{tr} has neither dynamical nor thermodynamical effects on the model and thereby does not influence the density of air, mass fluxes, latent heat release, or any other processes that are associated with water vapor. Because the climatological background flow fields are themselves not in a balanced state, it is necessary to add a forcing term to the model's equations to prevent them from evolving (Franzke et al. 2004; Yoo et al. 2012a). To acquire this forcing term, we initialize the model with the climatological fields and integrate the model forward by one time step. With the introduction of this forcing term, the modeled fields will only evolve when a perturbation is added to the climatological background fields. The perturbation we apply to the model experiment (EXP) is the heating rate

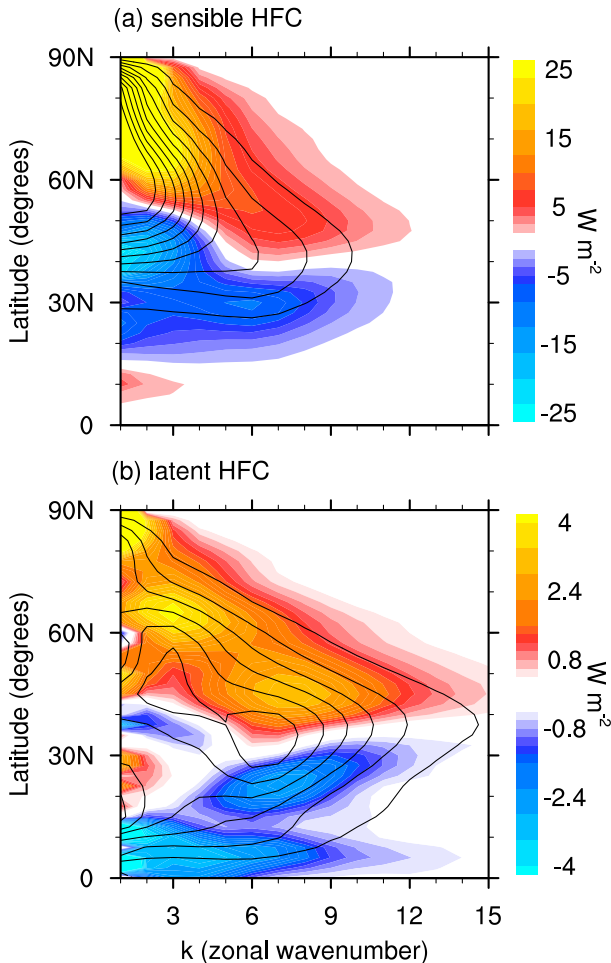


FIG. 1. DJFM climatological zonal means of (a) meridional sensible heat flux (contours; outermost contour and contour interval are $5 \times 10^6 \text{ W m}^{-2}$) and sensible HFC (shading) and (b) meridional latent heat flux (contours; outermost contour and contour interval are $1 \times 10^6 \text{ W m}^{-2}$) and latent HFC (shading) as functions of latitude and k . Calculated according to $-\nabla \cdot (c_p g^{-1} \int \mathbf{v}_k T_k dp)$ and $-\nabla \cdot (L_v g^{-1} \int \mathbf{v}_k q_k dp)$, respectively, where $\mathbf{v}_k = u_k \mathbf{i} + v_k \mathbf{j}$. Two iterations of nine-point local smoothing were applied before plotting. Derived from ERA-Interim (1979–2014) data.

h^* (K s^{-1}) that corresponds to the latent heat release associated with the composite of tropical convective precipitation P_{conv} (m s^{-1}) during the PSW life cycle. To create h^* , we adopt the methods of Yoo et al. (2012a), to which we refer the reader for further details.

Because EXP uses a DJFM climatological background flow for its initial state, there are no embedded shortwaves in the initial flow that would amplify into SSWs through baroclinic instability and reinforce the PSW anomaly. In fact, for such SSWs to develop, it would require the forcing in the tropics to propagate into and to

sufficiently stir the midlatitudes. Jin and Hoskins (1995) showed in a similar model with imposed tropical heating that it takes about two weeks for SSWs to develop through baroclinic instability. Also, because there is no diabatic heat release, any SSWs that develop would have to do so in the absence of diabatic energization (Willison et al. 2013). For these reasons, we expect that the agreement between EXP and the observed PSW life cycle will gradually deteriorate as the stirred wave propagates into higher latitudes. Therefore, discrepancies between EXP and PSW would augment the interpretation of the observational analyses that the SSWs play an important role in shaping the PSWs and ARs in the extratropics.

3. Observational analysis

We begin our observational analysis with a motivational figure that displays the climatological values of sensible and latent heat flux convergence (HFC) as functions of k and latitude during DJFM (Fig. 1; shading). There are two distinct dipoles in sensible HFC: one for PSWs where $k \approx 1\text{--}3$ and one for SSWs where $k \approx 5\text{--}7$ (Fig. 1a). The SSW dipole exhibits a maximum in divergence at $\sim 30^\circ\text{N}$ and a maximum in convergence at $\sim 50^\circ\text{N}$, while the PSW dipole resides farther north with peak values of divergence and convergence at $\sim 45^\circ$ and 70°N , respectively. With respect to latent HFC, there again exists an SSW dipole (Fig. 1b). However, compared to its sensible HFC counterpart, it subsumes higher wavenumbers, reflecting the important contribution by smaller-scale features in moisture transport. The stark difference in spatial scale between the sensible and latent heat transports can be interpreted from a quasigeostrophic (QG) framework where temperature can be scaled by streamfunction, which is selective toward larger horizontal scales. In contrast, to the extent that moisture may be regarded as a passive tracer field embedded in a nonsteady flow, it is expected to undergo chaotic filamentation (Aref 1984; Ottino 1990) and thereby project onto smaller horizontal scales.

PSW latent HFC displays peak values of divergence and convergence at $\sim 10^\circ$ and $\sim 65^\circ\text{N}$, respectively. Between these two centers, there appears a secondary center of divergence at $\sim 40^\circ\text{N}$ adjacent to two regions with less clear PSW signals. From Fig. 1, it is clear that the PSWs are instrumental in delivering heat and moisture into the Arctic, whereas the influence of the SSWs fades poleward of 60°N . To explain this fading influence, it may be argued that as an SSW with a conserved wavelength propagates poleward, spherical geometry requires its k to decrease, mathematically transforming it into a PSW. However, if spherical geometry accounts for the reduction in k , one would expect the dipoles in Fig. 1 to be

tilted from left to right with decreasing latitude. For example, if the $k = 2$ sensible HFC maximum at 70°N conserved its wavelength, then the sensible HFC minimum near 50°N would correspond to $k = 4$ or 5 . The absence of tilt for the sensible HFC dipole therefore implies that the planetary-scale dipoles in Fig. 1 are distinct from those at the synoptic scale. In addition, using ray tracing for a simple baroclinic model with a realistic background flow, Hoskins and Karoly (1981) showed that, while PSWs can propagate into the Arctic, SSWs fail to reach the Arctic as they undergo reflection equatorward of 60°N .

In Figs. 2a and 2b, we plot composites of the zonal means of anomalous SSW and PSW latent HFC during the PSW life cycle. Although SSW latent HFC shows little statistical significance, there are some signals worth mentioning (Fig. 2a). First, near lag day -3 , there is a divergence–convergence dipole straddling $\sim 35^\circ\text{N}$. This dipole matches the SSW climatology well (Fig. 1b) and therefore indicates a modest enhancement of SSW activity just before the peak of the PSW life cycle. By lag day 0, this dipole disappears, which suggests that there is a transfer of energy to larger scales that contributes to the growth of the PSWs. Near lag day 0 and centered at $\sim 45^\circ\text{N}$, a new dipole with anomalous convergence (divergence) to the south (north) develops and lasts ~ 7 days. This second dipole appears to fill a gap with no clear signal in PSW latent HFC near lag day 0 at $\sim 45^\circ\text{N}$ (Fig. 2b). This gap develops as a PSW divergence–convergence dipole, which first developed near lag day -7 , splits with the divergence (convergence) center propagating southward (northward). The propagation of these centers may be explained by the growth in amplitude, and thereby meridional extent, of the PSWs themselves. Furthermore, at lag day 0, the values of anomalous PSW latent HFC show overall agreement in sign at all latitudes with the PSW latent HFC climatology (Fig. 1b), suggesting the PSW life cycle reinforces the PSW climatology. Finally, Fig. 2c shows that the anomalous TCW during the PSW life cycle may largely be explained in the midlatitudes and the Arctic by the PSW latent HFC anomalies. The deficit in TCW over the tropics reflects that most PSW events occur during La Niña conditions (Lee 2012; BL15). Most remarkably, the positive TCW anomalies over the Arctic begin developing near lag day -5 and last more than two weeks, indicating a prolonged period of enhanced downward IR and surface warming.

We now investigate the presence and characteristics of ARs over the North Pacific during the PSW life cycle. Figures 3a and 3f collectively depict climatological values of \mathbf{Q}_r frequency (the percentage of days when \mathbf{Q}_r is nonzero), MSLP, and \mathbf{Q}_r during DJFM. There are maxima in \mathbf{Q}_r frequency along the North

Pacific storm track, the tropical easterlies, and north of 80°N because of the influence of spherical geometry on Eq. (1). The Siberian high and Aleutian low are both visible in the MSLP field. Encircling the Aleutian low, along its southern and eastern peripheries, \mathbf{Q}_r transports moisture east-northeastward across the North Pacific into the west coast of North America. Figures 3g–j depict anomalous values of MSLP and \mathbf{Q}_r during the PSW life cycle. Through the peak of the life cycle, the large-scale MSLP pattern exhibits a planetary-scale surface ridge centered over the Gulf of Alaska with a broad surface trough over western Russia. The ridge retrogrades westward while the Aleutian low amplifies to the south-southwest of the ridge. The surface winds induced by the anomalous MSLP field divert \mathbf{Q}_r to the north and west, through the Bering Strait into the Arctic. By lag days $+2$ – 4 , the center of the anomalous surface ridge resides over the Bering Strait and blocks any additional flow of moisture into the Arctic. Figures 3b–e depict anomalous values of \mathbf{Q}_r frequency during the PSW life cycle. Throughout the life cycle, there are positive anomalies of \mathbf{Q}_r frequency over the Bering Strait. When added to the climatology, these positive anomalies imply a total \mathbf{Q}_r frequency of $\sim 25\%$ on any individual lag day during the PSW life cycle. Through the peak of the life cycle, positive anomalies develop between Hawaii and the southern Alaskan coast while negative anomalies manifest over the west coast of North America. These anomalies represent a backing of the climatological \mathbf{Q}_r from a southwesterly to a southerly flow, resulting in anomalous moisture transport through the Bering Strait into the Arctic. It is worth noting that, on lag days $+2$ – 4 , \mathbf{Q}_r frequency remains anomalously positive over the Arctic despite the transport of moisture being blocked by the ridge over the Bering Strait. This result coincides well with the anomalously high TCW that persists following the peak in the PSW life cycle (Fig. 2c). Finally, the climatological \mathbf{Q}_r reestablishes itself over the west coast of North America, quickly following the peak of the PSW life cycle.

To gain insight on the vertical structure of the moisture intrusions into the Arctic during the PSW life cycle, Fig. 4 displays a composite of the anomalous values of total northward water vapor flux vq (shading), superimposed on the DJFM climatological values of vq (contours). We focus on the fluxes through 65°N over the Pacific sector. Although the greatest fluxes reside in the lower troposphere, statistically significant fluxes occur throughout the entire troposphere near the Bering Strait during negative lags and the peak of the life cycle. The greatest

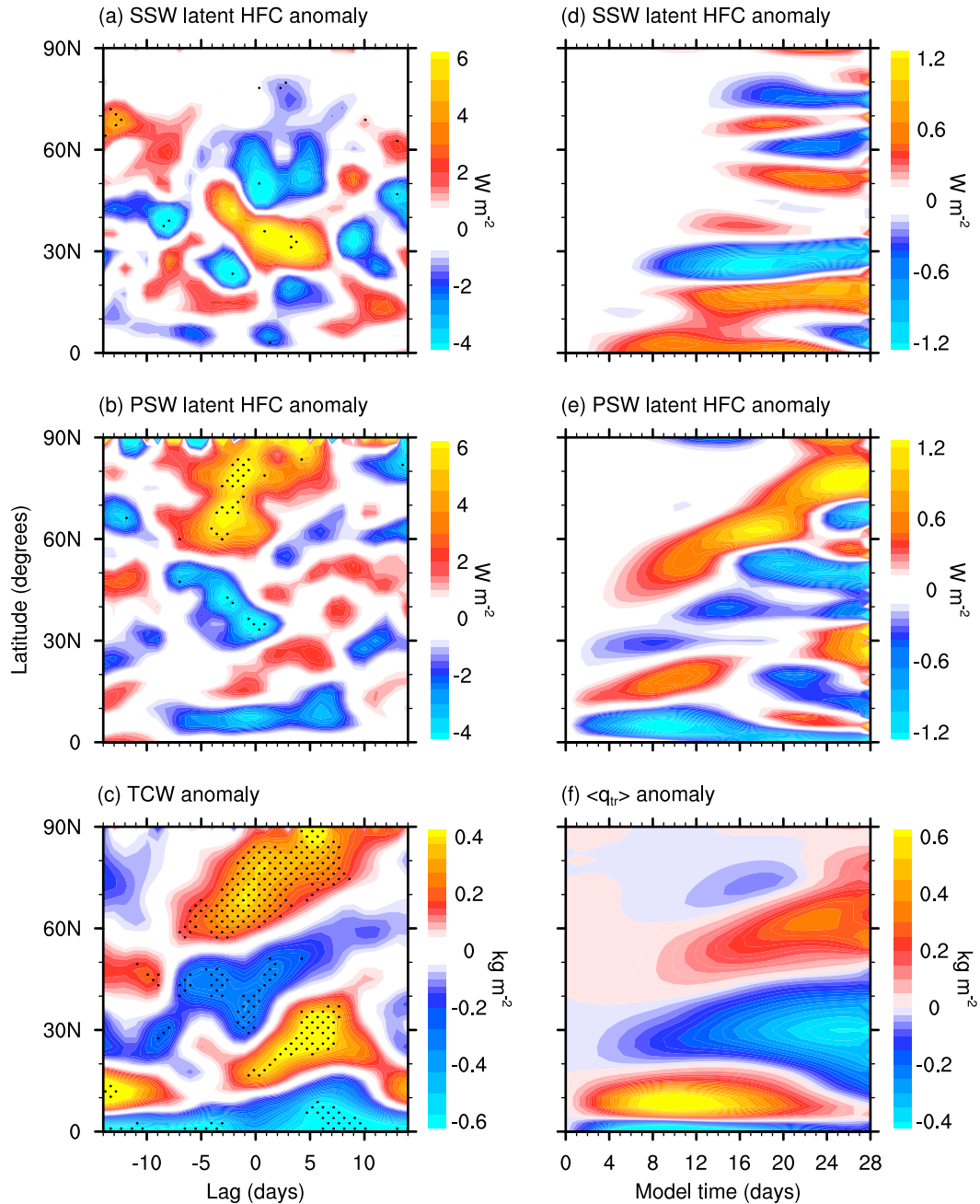


FIG. 2. Composites of the zonal means of anomalous (a) shortwave latent HFC, (b) longwave latent HFC, and (c) TCW during the PSW life cycle ($n = 34$ events). Dotted areas indicate statistical significance at the 5% level, evaluated via a Monte Carlo simulation with 1000 random samples. Derived from ERA-Interim (1979–2014) data. Model output of the zonal means of anomalous (d) shortwave latent HFC, (e) longwave latent HFC, and (f) $\langle q_{tr} \rangle$ during EXP. Values in (a), (b), (d), and (e) are calculated according to $-\nabla \cdot (L_v g^{-1} \int \mathbf{v}_k \overline{q_k} dp)$, where $\mathbf{v}_k = u_k \mathbf{i} + v_k \mathbf{j}$. In (a) and (d), $k \geq 4$ are used, $k = 1-3$ are used for (b) and (e), and q_{tr} is substituted for q in (d) and (e). Two iterations of nine-point local smoothing were applied before plotting.

anomalous fluxes exist to the west of the largest climatological values and retrograde westward by lag day 0 (cf. Figs. 4a,d). At positive lags, the fluxes quickly recede toward climatological values (Fig. 4e).

These fluxes by vq are consistent with the fluxes by Q_r , depicted in Fig. 3 and suggest that the anomalous fluxes by vq are largely driven by the anomalous fluxes by Q_r . In fact, we find (not shown here) that the

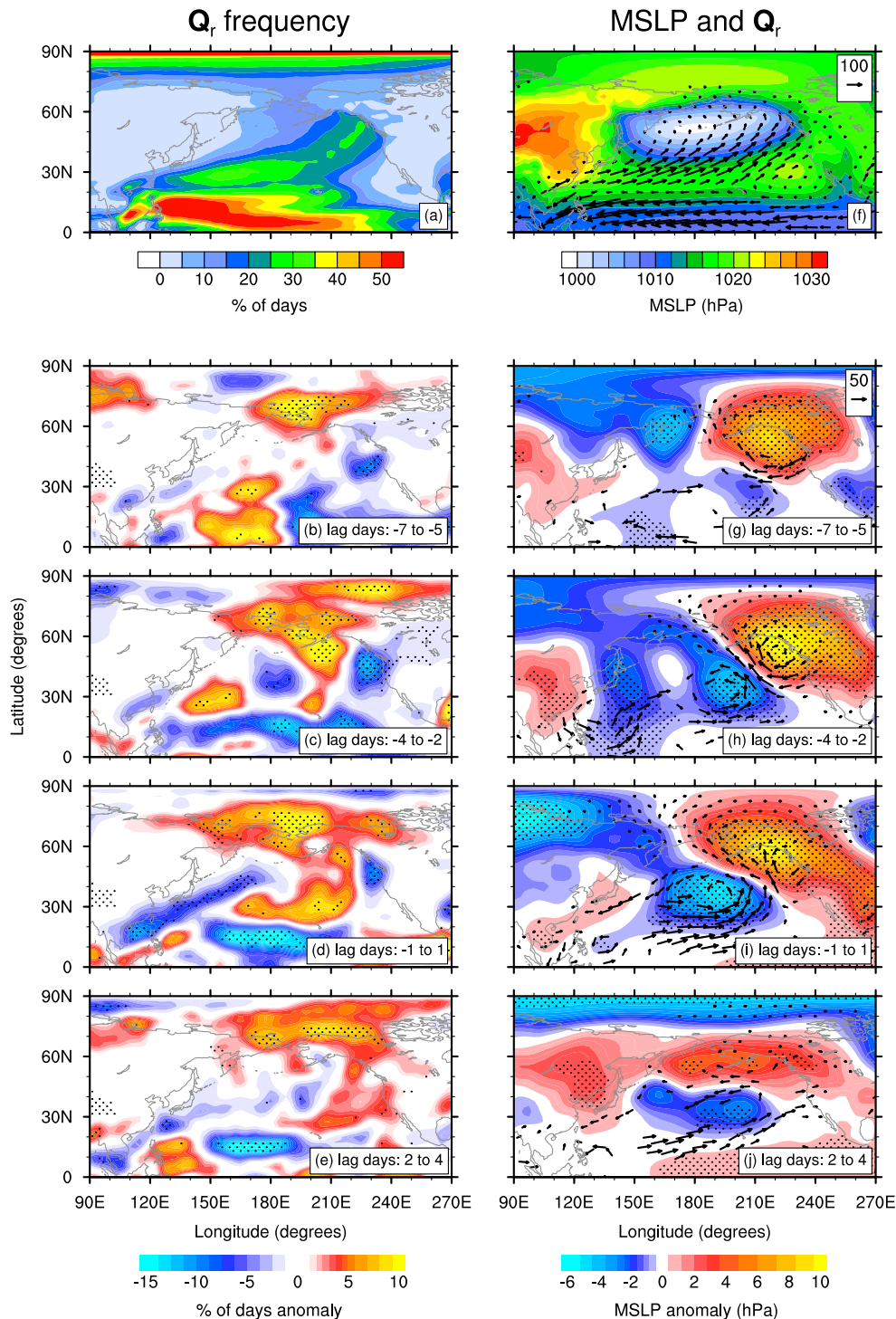


FIG. 3. (a) Percentage of all DJFM days from 1979 to 2014 when $Q_r \neq 0$. (b)–(e) Composite of the anomalous percentage of days when $Q_r \neq 0$ during the PSW life cycle ($n = 34$ events). For example, over the Bering Strait, (a) shows that Q_r exists $\sim 10\%$ – 15% of all DJFM days, whereas (d) shows that Q_r exists an additional $\sim 10\%$ of the days spanning from lag day -1 to lag day $+1$ across all PSW life cycle events. This implies that Q_r exists $\sim 20\%$ – 25% of the time over the Bering Strait during the peak of the PSW life cycle. (f) DJFM climatological MSLP and Q_r . (g)–(j) Composites of anomalous MSLP and anomalous Q_r during the PSW life cycle. Reference vectors ($\text{kg m}^{-1} \text{s}^{-1}$) are shown in the upper right of (f) and (g). For (f)–(j), only vectors with $Q_r \geq 5 \text{ kg m}^{-1} \text{s}^{-1}$ are shown. Additionally, for (g)–(j) only vectors with either component statistically significant at the 5% level are shown. Dotted areas indicate statistical significance at the 5% level. All statistical significance is evaluated via a Monte Carlo simulation with 1000 random samples. Two iterations of nine-point local smoothing were applied to (b)–(e) before plotting. Derived from ERA-Interim (1979–2014) data.

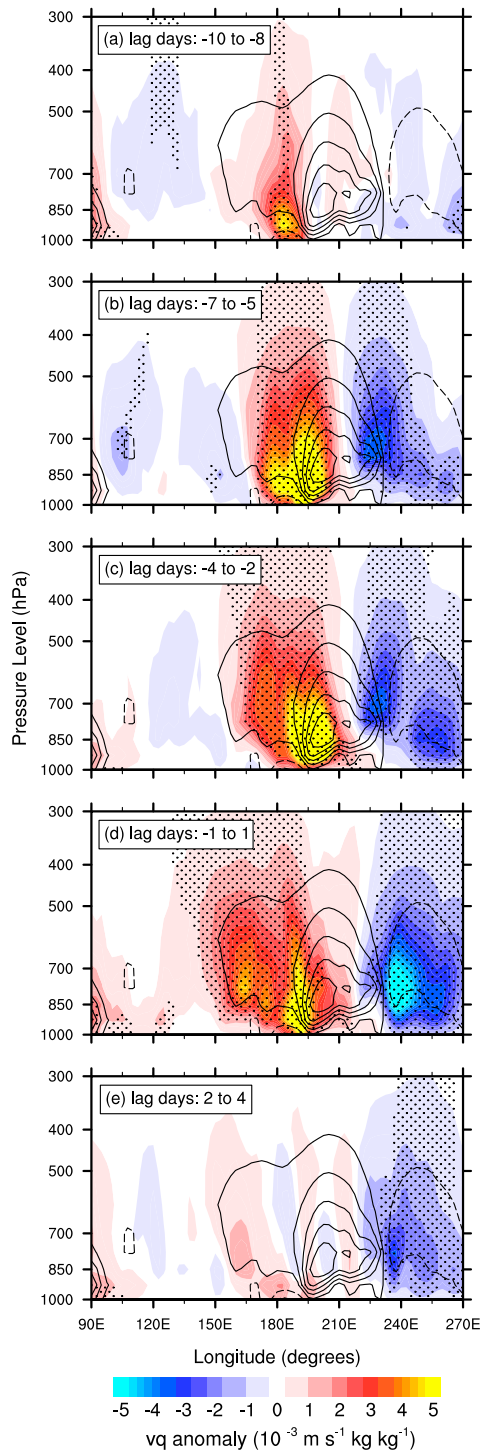


FIG. 4. Composite of the anomalous total northward water vapor flux vq along 65°N during the PSW life cycle (shading; $n = 34$ events). Black contours depict the climatological vq during DJFM. The contour interval is $1 \times 10^{-3} \text{ m s}^{-1} \text{ kg kg}^{-1}$. Solid (dashed) lines represent positive (negative) values; the zero contour is omitted. Dotted areas indicate statistical significance at the 5% level, evaluated via a Monte Carlo simulation with 1000 random samples. Derived from ERA-Interim (1979–2014) data.

northward transport of moisture by \mathbf{Q}_r through 65°N between 90° and 270°E near the peak of the PSW life cycle is essentially equal to the transport by \mathbf{Q}_t , reaching a value of $\sim 0.71 \times 10^8 \text{ kg s}^{-1}$. This transport is much larger than the DJFM climatological northward transports of $\sim 0.24 \times 10^8$ and $0.30 \times 10^8 \text{ kg s}^{-1}$ by \mathbf{Q}_r and \mathbf{Q}_t , respectively. These values are consistent with previous studies that find ARs account for a substantial majority of the total poleward moisture transport in the midlatitudes (Zhu and Newell 1998; Newman et al. 2012; Guan and Waliser 2015).

To illustrate more concretely the synoptic-scale features that are present during the PSW life cycle, we present a particular PSW event that peaked in intensity on 01 December 2007. Figures 5a–f depict anomalous MSLP and total \mathbf{Q}_r for lag days -4 through $+1$ during the event’s life cycle. Similar to the composite (Fig. 3), an anomalous planetary-scale surface ridge (trough) exists in the eastern (western) North Pacific throughout the life cycle. This anomalous MSLP pattern steers \mathbf{Q}_r northward through the Bering Strait into the Arctic. In contrast to the composite, this event shows distinct minima in MSLP, corresponding to individual, synoptic-scale cyclones, rotating through the planetary-scale trough (Figs. 5a,b,d). These cyclones and their attendant cold fronts converge and steer the low-level moisture, forming \mathbf{Q}_r . In turn, the large-scale flow and downstream blocking steer the cyclones themselves northward. By lag day $+1$ (Fig. 5f), the anomalous surface ridge has diminished while retrograding westward, beginning to block any additional moisture from entering the Arctic. However, once having entered the Arctic, \mathbf{Q}_r is first steered westward (Fig. 5e) and then eastward (Fig. 5f), which allows for basinwide mixing of the warm, moisture-laden air with the cold, dry Arctic air mass. Meanwhile, to the south of the ridge, a series of three cyclones advances eastward toward the west coast of North America. Finally, we note that this event appears to have a tropical connection, with \mathbf{Q}_r winding from the Maritime Continent and through the Bering Strait. However, since Fig. 5 presents an Eulerian perspective, we cannot say with certainty that \mathbf{Q}_r transports moisture from the tropics to the Arctic. Rather, we must employ a Lagrangian backward trajectory analysis to gain insight on the pathways and moisture source regions of parcels entering the Arctic.

In Fig. 6, we employ HYSPLIT to plot 11 backward trajectories associated with ARs entering the Arctic during the PSW life cycle. We choose the 11 with the greatest values of \mathbf{Q}_r of the 32 ARs identified by the algorithm presented in section 2a(4). These 11

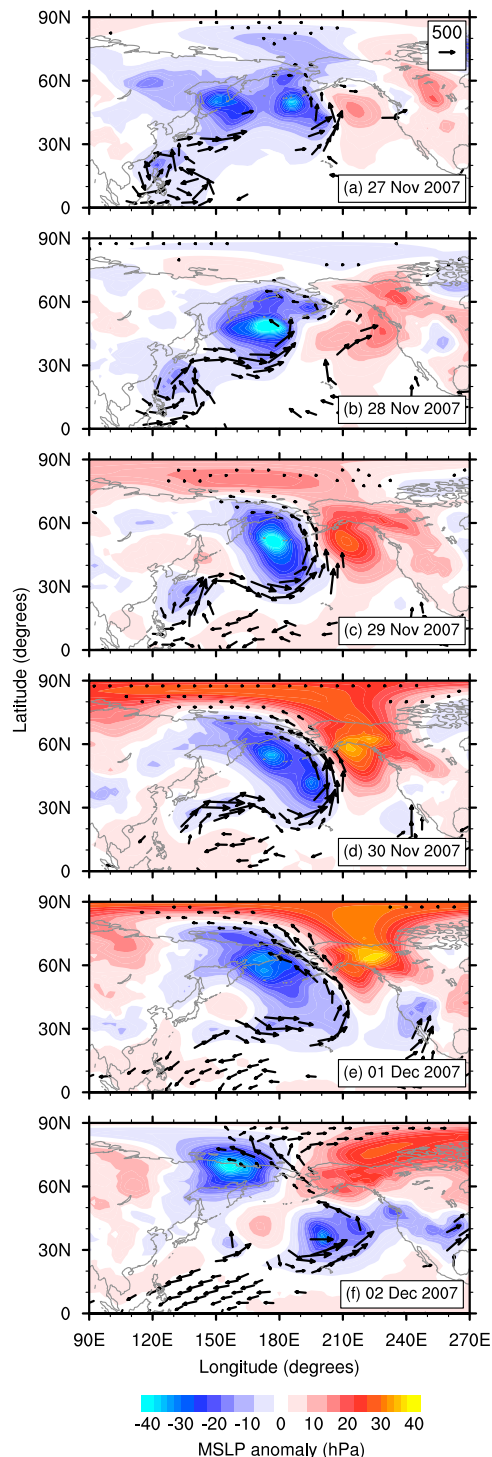


FIG. 5. (a)–(f) Anomalous MSLP and total \mathbf{Q} , during a PSW life cycle event whose EKE peaked at 0000 UTC 01 Dec 2007, with data from 0000 UTC 27 Nov 2007 through 0000 UTC 02 Dec 2007, respectively. Reference vector ($\text{kg m}^{-1}\text{s}^{-1}$) shown in the upper right of (a). Derived from ERA-Interim (1979–2014) data.

trajectories include the 1 December 2007 event (Fig. 5), which may be identified by the closed red circles along its route. We only show 11 of the 32 trajectories in order to present a less cluttered plot; the remaining trajectories share the same qualitative features that we identify in the top 11. We concentrate our analysis on the parcels with starting elevations between 2500 and 9000 m because these parcels are more likely to reach the southernmost latitudes and thereby reveal possible tropical source regions of moisture. For simplicity, we only depict the results from 4000 m, as the other trajectories with mid- and upper-tropospheric starting elevations have similar qualitative features. Figure 6a shows p of the parcels along their trajectories. We find that most of the parcels begin their northward journey at ~ 900 hPa before rising to ~ 600 hPa (4000 m). Because the top of the marine boundary layer typically resides between ~ 900 and 950 hPa (Knippertz and Wernli 2010), it is conceivable that these parcels entrain moisture rich air from the boundary layer along the southernmost extents of their trajectories, between $\sim 15^\circ$ and 35°N . Furthermore, we emphasize the speed at which the parcels move northward by plotting closed circles at 24-h intervals along each trajectory and find transport from the subtropics to high latitudes occurs in ~ 2 days.

Looking at relative humidity (Fig. 6b), we see that the parcels become increasingly saturated as they travel northward and experience adiabatic cooling during their ascent. A slow rise in θ along the trajectories suggests the release of latent heat as water vapor condenses (Fig. 6c). Interestingly, although θ increases, Fig. 6d reveals that θ_E decreases. Because θ_E is conserved if a parcel loses its moisture to precipitation, a decrease in θ_E implies that a parcel's water vapor mixing ratio must be decreasing as a result of nonconservative processes, such as mixing with the environmental air. This likely occurs as these warm, moist air masses rise along isentropic surfaces within warm conveyor belts and lose heat and moisture as they mix with the underlying cold, dry air masses. However, despite the parcels losing heat via mixing and presumably through cloud-top radiative cooling, it is worth emphasizing again that θ is increasing along the trajectories. This underscores the importance of latent heat release in warming both the parcels and their environment.

In Fig. 6e, we see that surface precipitation occurs along the northern extent of each parcel's trajectory, implying that surface evaporation is not significant at these times (Stohl and James 2004). To confirm this point, we plot the surface evaporation rate minus the

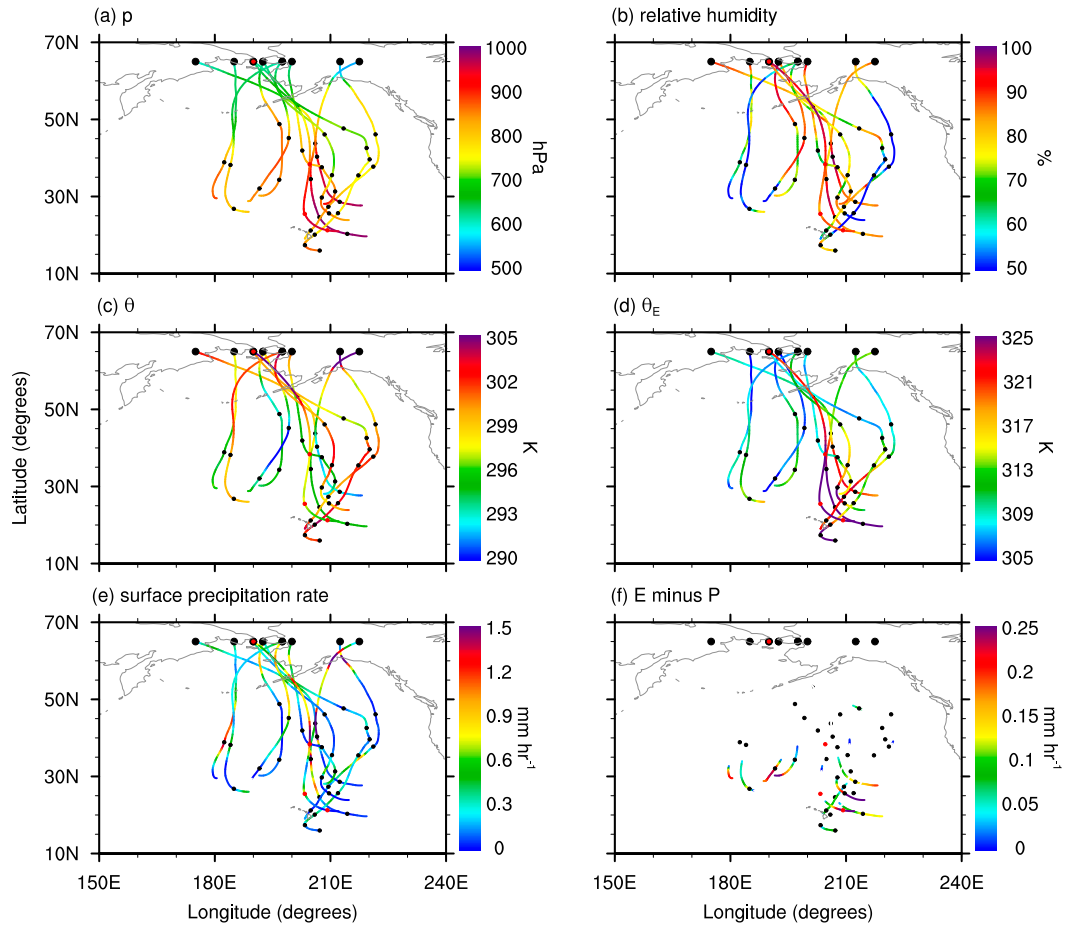


FIG. 6. Shown are 11 selected backward trajectories calculated via HYSPLIT of Q_r intrusions into the Arctic during PSW life cycle events. All trajectories are initialized at 4000 m and 65°N. Initial longitudes and times correspond to a given event's peak Q_r . See section 2a(4) for additional selection criteria. Displayed along each trajectory are the (a) pressure, (b) relative humidity, (c) θ , and (d) θ_E of the tracked parcel. (e) Surface precipitation rate. (f) Surface evaporation rate minus surface precipitation rate (E minus P). White segments along the trajectories in (f) indicate negative values of E minus P . Large black circles correspond to the location where each trajectory is initialized. Small black circles are placed at 24-h intervals along each trajectory. Each trajectory is only plotted to the southernmost latitude that it reaches before turning to the north again. The trajectory with red circles corresponds to the PSW life cycle event that peaks at 0000 UTC 01 Dec 2007. Derived from ERA-Interim (1979–2014) data.

surface precipitation rate (Fig. 6f) and find the preponderance of positive values exists over the subtropics (white gaps in the trajectories indicate negative values). We conclude that the most probable moisture source for the parcels entering the Arctic between 2500 and 9000 m is the subtropics, where the parcels are unsaturated, closest to the marine boundary layer, and evaporation at the surface exceeds precipitation. This conclusion agrees with the results of Gimeno et al. (2015), who identified non-tropical source regions over the North Pacific as being important for moisture in the Arctic over the East Siberian Sea. Despite a probable subtropical moisture source, we cannot dismiss the likelihood that moisture

derives from higher latitudes (Sodemann and Stohl 2013), particularly for parcels that enter the Arctic at lower elevations. Moreover, moisture may be horizontally converged into the ARs from neighboring source regions that experience local evaporation or from in situ convection, which is not resolved well at ERA-Interim's resolution. However, the decline in θ_E along the trajectories suggests that the above two processes, inasmuch as they occur, are less important than the net drying of the parcel through its mixing with environmental air.

We now connect the results presented in this study with those recently presented by Woods et al. (2013) and Liu and Barnes (2015). These studies showed that extreme

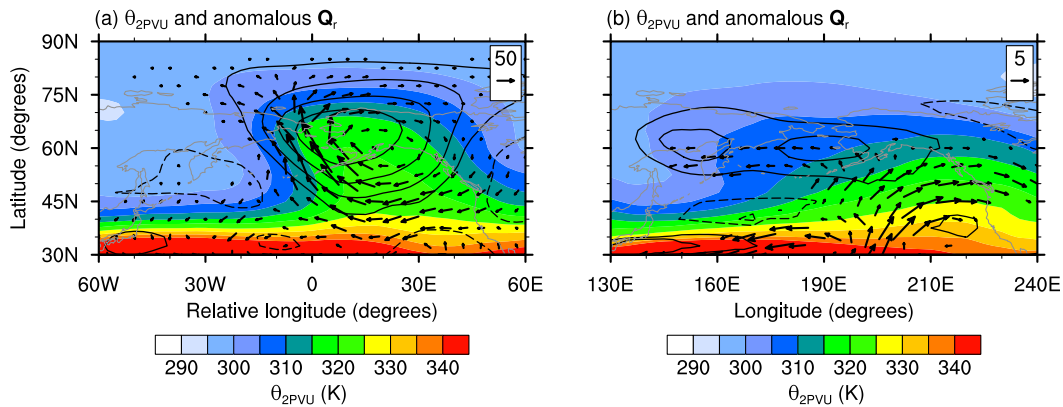


FIG. 7. (a) Composite of total θ_{2PVU} and anomalous Q_r , averaged from lag day -1 to lag day $+1$ of Q_r intrusions into the Arctic during PSW life cycle events ($n = 32$ events). The composite is made after shifting each event in time and longitude such that each event is centered on its peak Q_r at 65°N . See the [section 2a\(4\)](#) for additional selection criteria. Two iterations of nine-point local smoothing were applied before plotting. Derived from ERA-Interim (1979–2014) data. (b) Model output of total θ_{2PVU} and anomalous Q_r , averaged over model days 13–15 during EXP. Model output anomalous Q_r is calculated by applying Eq. (1) to the model output anomalous Q_r . Reference vectors ($\text{kg m}^{-1} \text{s}^{-1}$) are shown in the upper right of (a) and (b). Only vectors with $Q_r \geq 5 \text{ kg m}^{-1} \text{s}^{-1}$ and $Q_r \geq 0.5 \text{ kg m}^{-1} \text{s}^{-1}$ are shown for (a) and (b), respectively. Black contours depict anomalous θ_{2PVU} with contour intervals of 3 and 0.3 K for (a) and (b), respectively. Solid (dashed) lines represent positive (negative) anomalies; the zero contour is omitted.

moisture intrusions into the Arctic from the North Pacific basin are associated with downstream blocking and cyclonic Rossby wave breaking by examining fields of θ_{2PVU} . The θ_{2PVU} surface resides very close to the tropopause in the extratropics and may be used to diagnose Rossby wave breaking (Franzke et al. 2011; Liu and Barnes 2015). From a potential vorticity perspective (Hoskins et al. 1985), one would expect Rossby wave breaking near the tropopause to influence the MSLP field and thereby redirect moisture transport. We tie our results to Fig. 4c of Liu and Barnes (2015) by plotting composites of θ_{2PVU} and anomalous Q_r in Fig. 7a. Rather than compositing these fields on lag day 0 of the PSW life cycle, we perform a temporal and spatial shift on each event before compositing. We center the composite on the day that corresponds to when the 32 ARs identified in section 2a(4) cross into the Arctic, and shift each event onto a common longitude. Figure 7a reveals the total θ_{2PVU} field to be nearly identical to that in Liu and Barnes (2015). Essentially, there is a meridional overturning of total θ_{2PVU} with the adjacent troughs and ridges tilted in a northwest-to-southeast fashion, indicative of cyclonic Rossby wave breaking (Thorncroft et al. 1993; Franzke et al. 2011). To the west-southwest of the largest positive θ_{2PVU} anomaly, we find that Q_r exhibits its largest northward component. Furthermore, Franzke et al. (2011) identified the importance of cyclonic Rossby wave breaking in the building of the positive phase of the Pacific–North America teleconnection pattern. They

found that cyclonic Rossby wave breaking in the North Pacific was favored following enhanced tropical convection in the western Pacific, near the Maritime Continent. Therefore, the extreme moisture intrusions found here and in the aforementioned studies are likely linked to PSW dynamics where tropical convection plays a central role in amplifying the PSWs. We test this hypothesis using an idealized model in section 4.

To conclude our observational analysis, we composite and display on a skew- T diagram the vertical profiles of T , dewpoint temperature T_d , u , and v (Fig. 8). The composite is centered in time and longitude in a manner identical to Fig. 7a. We advise caution in interpreting the lowest levels of the atmosphere because surface pressures at high latitudes are oftentimes greater than 1000 hPa. In fact, radiosonde data from Arctic stations show a very complex boundary layer, with steep, shallow inversions that lie beneath the 1000-hPa surface. For this reason, the planetary boundary layer may not be accurately represented in Fig. 8. Nevertheless, we observe several interesting features. Beginning on lag day -11 we see a relatively dry and cold troposphere with T near -20°C at 1000 hPa, underneath an inversion that exists up to 850 hPa. The vertical wind profile shows light northeasterlies near the surface and calm winds aloft. Progressing through lag day 0, the entire troposphere warms and moistens as southerly winds strengthen aloft and surface winds veer southeasterly. Indeed, the vertical wind profile veers with height,

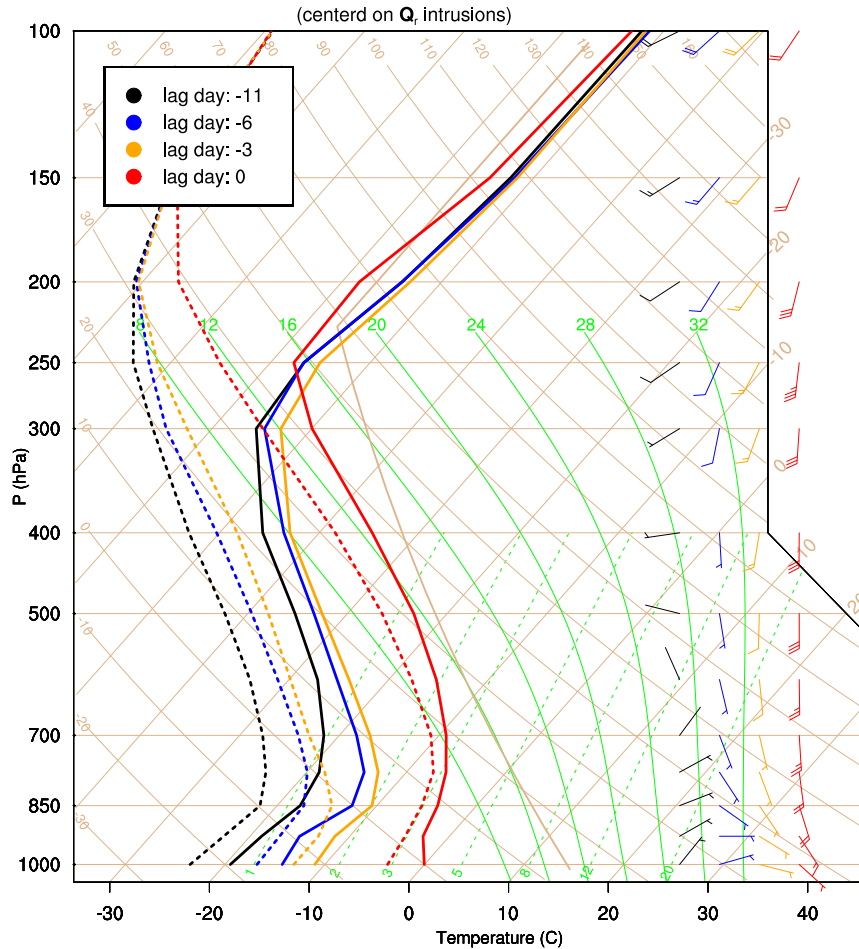


FIG. 8. Composite skew T of Q_r intrusions into the Arctic during PSW life cycle events ($n = 32$ events). The composite is made after shifting each event in time and longitude such that each event is centered on its peak Q_r at 65°N . See section 2a(4) for additional selection criteria. Four selected lag days are shown: -11 , -6 , -3 , and 0 in black, blue, yellow, and red, respectively. Solid (dashed) lines represent T (T_d). Wind bars on the right, with half lines and full lines representing 5 and 10 m s^{-1} intervals, respectively. Derived from ERA-Interim (1979–2014) data.

indicative of warm air advection. Remarkably, on lag day 0, T has reached 0°C at 1000 hPa, while the surface inversion has completely eroded. Furthermore, the proximity of the T and T_d profiles to each other suggests a cloudy, precipitating atmosphere—a conclusion supported by Fig. 6e. On lag day +6 (not shown here), we see the surface inversion begin to reestablish itself, while lower-tropospheric values of T and T_d remain elevated by $\sim 2^\circ\text{C}$ compared to their values seen on lag day -6 . This is consistent with the positive TCW anomalies (Fig. 2c) and positive 2-m temperatures (Fig. 4a of BL15) observed following the peak of the PSW life cycle. Furthermore, the positive T and T_d anomalies, seen before and after the moisture intrusions, contribute to enhanced downward IR

(Doyle et al. 2011; Kapsch et al. 2013; Flournoy et al. 2016). Inasmuch as basinwide mixing of the warm, moisture-laden air with the cold, dry Arctic air occurs (Figs. 2c, 5e–f, 6d), the enhanced downward IR can lead to surface warming throughout the entire Arctic.

4. Model analysis

In this section, we perform EXP to test the hypothesis that localized tropical convection can lead to the development of PSWs that transport moisture into the Arctic. We perturb the model with an h^* that corresponds to the composite of the 5-day average of anomalous P_{conv} seen during the PSW life cycle,

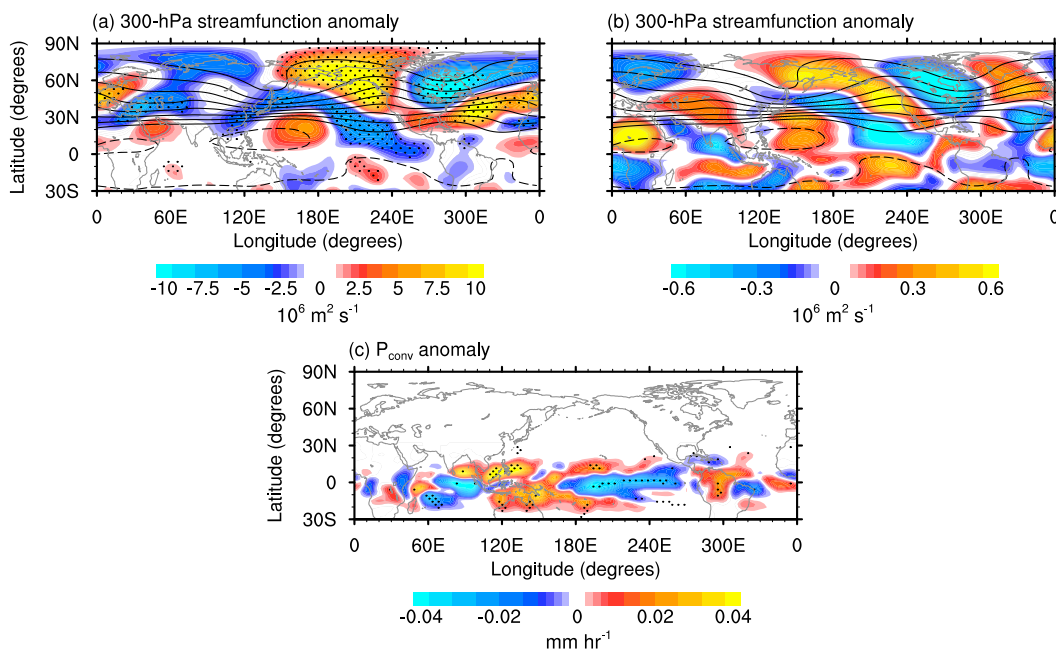


FIG. 9. (a) Composite of anomalous 300-hPa streamfunction averaged from lag day -1 to lag day $+1$ of the PSW life cycle ($n = 34$ events). (b) Model output of anomalous 300-hPa streamfunction averaged over model days 13–15 during EXP. Zonal means of the anomalous 300-hPa streamfunction have been removed before plotting both (a) and (b). In (a) and (b) black contours depict the climatological 300-hPa streamfunction during DJFM. The contour interval is $15 \times 10^6 \text{ m}^2 \text{ s}^{-1}$. Solid (dashed) lines represent negative (positive) values; the zero contour is omitted. (c) Composite of anomalous P_{conv} averaged from lag day -14 to lag day -10 during the PSW life cycle, tapered away from the equator according to a cosine squared weighting function (see section 2b). The composite (c) is used to determine h^* in EXP. Dotted areas in (a) and (c) indicate statistical significance at the 5% level, evaluated via a Monte Carlo simulation with 1000 random samples. Two iterations of nine-point local smoothing were applied to (c) before plotting. Derived from ERA-Interim (1979–2014) data.

centered on lag day -12 . We set h^* to increase linearly from zero to its full value on day 1, to be stationary for the next 8 days, and to decrease linearly back to zero on day 10. We conduct various sensitivity tests by changing the number of lag days to average, the lag day to center the average on, and the number of days h^* is stationary. We also try varying h^* to correspond with the observed evolution of P_{conv} during the PSW life cycle. We find that a large suite of the tests, whose h^* is predominantly a function of P_{conv} from approximately lag day -10 to lag day -14 , produce qualitatively similar results. Thus, we choose to present here only the model results from the parameterization of h^* as described above.

Figure 9a depicts the composite of the anomalous 300-hPa streamfunction observed from lag day -1 to lag day $+1$ of the PSW life cycle. We subtract the zonal mean at each latitude to emphasize the wave structure. A Rossby wave train is visible, arching northeastward through the North Pacific before reaching its turning latitude over North America and returning

equatorward via the Atlantic. The net result of this wave pattern is to constructively interfere with, and thereby amplify, the DJFM climatological stationary waves. Interestingly, the center of the upper-level ridge over western Alaska resides slightly west of the surface ridge seen in Fig. 3i, which alludes to the baroclinic nature of these PSWs (BL15) and their contribution to poleward eddy heat flux. Moreover, the upper-level flow shows enhanced southerly flow over both the North Pacific and North Atlantic, an ideal pattern for the transport of moisture into the Arctic. Figure 9b shows EXP's anomalous (departure from DJFM climatology) 300-hPa streamfunction pattern, averaged over model days 13–15, in response to h^* corresponding to the anomalous P_{conv} shown in Fig. 9c. The observed and modeled 300-hPa streamfunction patterns are remarkably similar over the North Pacific, with pattern correlations between these two quantities peaking at 0.44 for the entire Northern Hemisphere on model day 13 and 0.69 for the Northern Hemisphere between 120° and 300°E on model day 14. The results

of EXP suggest that P_{conv} drives the development of the PSWs. Indeed, the positive anomalies of P_{conv} over the Maritime Continent are ideally located to produce upper-level divergence that interacts with the tight absolute vorticity gradient of the East Asian subtropical jet. This interaction produces a Rossby wave source that excites a Rossby wave train that propagates northeastward and reaches the Arctic ~ 10 days later (Hoskins and Karoly 1981; Sardeshmukh and Hoskins 1988), a timing consistent with the forcing and subsequent model response seen in EXP.

We use q_{tr} in EXP to compute the zonal means of the SSW latent HFC anomaly (Fig. 2d), PSW latent HFC anomaly (Fig. 2e), and the vertically integrated tracer anomaly $\langle q_{\text{tr}} \rangle$ (Fig. 2f) found over the 28-day model run. Comparing these figures to their counterparts observed during the PSW life cycle (Figs. 2a–c), we see both similarities and differences. With respect to the SSW latent HFC anomaly, we see the model bears little resemblance to the PSW life cycle composite, particularly over the midlatitudes. Indeed, the model does not produce anomalies north of the subtropics until near model day 14. This muted SSW activity is not entirely unexpected for the reasons enumerated in section 2b. Figure 7b shows additional evidence for the absence of SSW activity in the model by revealing that total $\theta_{2\text{PVU}}$ does not overturn as it does in observations, suggesting a lack of synoptic-scale cyclonic Rossby wave breaking. Consequently, the $\theta_{2\text{PVU}}$ anomalies are only slightly positive over eastern Russia and the Bering Strait in the model. Furthermore, anomalous \mathbf{Q}_r (for a definition of anomalous \mathbf{Q}_r with respect to EXP, see the caption to Fig. 7) is only slightly diverted northwest in the model, with larger anomalies directed to the west coast of North America. These small anomalies contrast starkly with the warm and moist intrusion seen in observations (Fig. 7a). Therefore, to the extent that an upscale energy cascade amplifies the PSWs during the observed PSW life cycle, the model's muted SSW activity may hinder the amplification of PSWs.

Returning our attention to Fig. 2, we see that the PSW latent HFC anomaly in EXP resembles the PSW life cycle composite, with prominent convergence existing at high latitudes and divergence in the midlatitudes. This may be seen by comparing EXP's anomalies after model day 16 (Fig. 2e) with those from the PSW life cycle between lag days -5 and $+2$ (Fig. 2b). Consistent with the PSW life cycle, beginning near model day 20, the convergence–divergence dipole appears to separate over the remainder of the model run. However, in contrast to the PSW life cycle, the values of convergence penetrate the Arctic more

slowly. Figure 2f shows the $\langle q_{\text{tr}} \rangle$ anomaly in the model. Because q_{tr} is a passive tracer, it neither condenses nor precipitates, which makes it more analogous to TCW than to TCW vapor in the observed atmosphere. Positive anomalies of $\langle q_{\text{tr}} \rangle$ develop over the high latitudes several days after the peak values in the PSW latent HFC are seen, consistent with the observed PSW life cycle (Figs. 2b,c).

Figure 10a shows the composite of the TCW anomaly observed for lag days from -1 to $+1$ of the PSW life cycle, while Fig. 10b shows EXP's $\langle q_{\text{tr}} \rangle$ anomaly averaged over model days 13–15. Both figures also depict total \mathbf{Q}_r stretching east-northeastward from the Maritime Continent. Whereas the PSW life cycle shows a diversion of \mathbf{Q}_r to the north over the central North Pacific, the model shows \mathbf{Q}_r impinging on the west coast of North America without any diversion northwestward, despite the positive $\langle q_{\text{tr}} \rangle$ anomalies that exist along the southern coast of Alaska. In EXP, the positive $\langle q_{\text{tr}} \rangle$ anomalies do not penetrate the highest latitudes, as seen in the observed TCW anomalies. Regardless, the model result does show the importance of tropical convection amplifying the PSWs in such a manner as to create a large-scale pathway for the poleward transport of moisture to high latitudes. In fact, any SSW activity impinging on the positive $\langle q_{\text{tr}} \rangle$ anomalies in the subtropics would likely converge moisture along their attendant frontal zones, channeling moisture northward in a more direct fashion through the Bering Strait into the Arctic, as actually observed during the PSW life cycle.

5. Conclusions

In this study we performed both observational and model analyses to examine the role that SSWs and ARs play in the poleward transport of moisture into the Arctic during the PSW life cycle. The schematic in Fig. 11 summarizes our key findings, presented in order of occurrence during the PSW life cycle:

- 1) Localized tropical convection over the Maritime Continent exists ~ 10 – 14 days before the peak of the PSW life cycle. The importance of this convection in developing the PSW life cycle is confirmed with an idealized model by perturbing a climatological DJFM background flow with heating that corresponds to the latent heat released by this tropical convection.
- 2) The upper-level divergent wind produced by the tropical convection interacts with the subtropical jet exiting Southeast Asia, producing a Rossby wave source.
- 3) The subsequent Rossby wave train arches northeastward over the North Pacific before returning

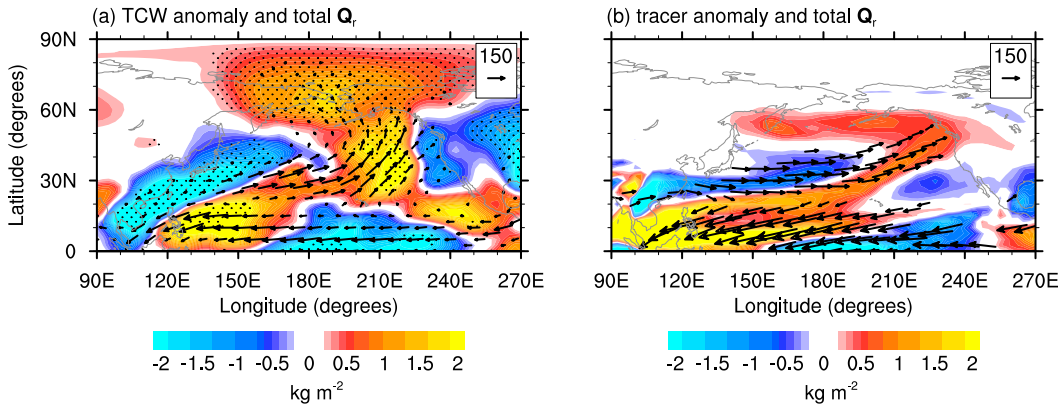


FIG. 10. (a) Composite of anomalous TCW and total Q_r , averaged from lag day -1 to lag day $+1$ of the PSW life cycle ($n = 34$ events). Two iterations of nine-point local smoothing were applied before plotting. Dotted areas indicate statistical significance at the 5% level, evaluated via a Monte Carlo simulation with 1000 random samples. Derived from ERA-Interim (1979–2014) data. (b) Model output of anomalous $\langle q_{tr} \rangle$ and total Q_r , averaged over model days 13–15 during EXP. Reference vectors ($\text{kg m}^{-1} \text{s}^{-1}$) are shown in the upper right of (a) and (b). Only vectors with $Q_r \geq 15 \text{ kg m}^{-1} \text{s}^{-1}$ are shown.

equatorward over the North Atlantic. The Rossby wave train constructively interferes with the climatological DJFM stationary waves, thereby amplifying the PSWs. These PSWs are baroclinic and are ideally situated to transport sensible and latent heat into the Arctic through the Bering Strait (BL15).

- 4) Embedded within the PSWs, SSWs are diverted northward by the planetary-scale flow. The SSWs converge moisture along their trailing cold fronts over the subtropics. The moisture is channeled

northward and rises within the warm conveyor belts of the SSWs in the form of ARs. Upon reaching the Arctic the moisture branches eastward and westward, mixing with the ambient Arctic air, increasing both T and TCW values throughout the Arctic.

- 5) The SSWs undergo cyclonic Rossby wave breaking near the Bering Strait, which further amplifies the PSWs and enhances warm and moist air advection into the highest latitudes of the Arctic. This process ceases when the planetary-scale ridge located over

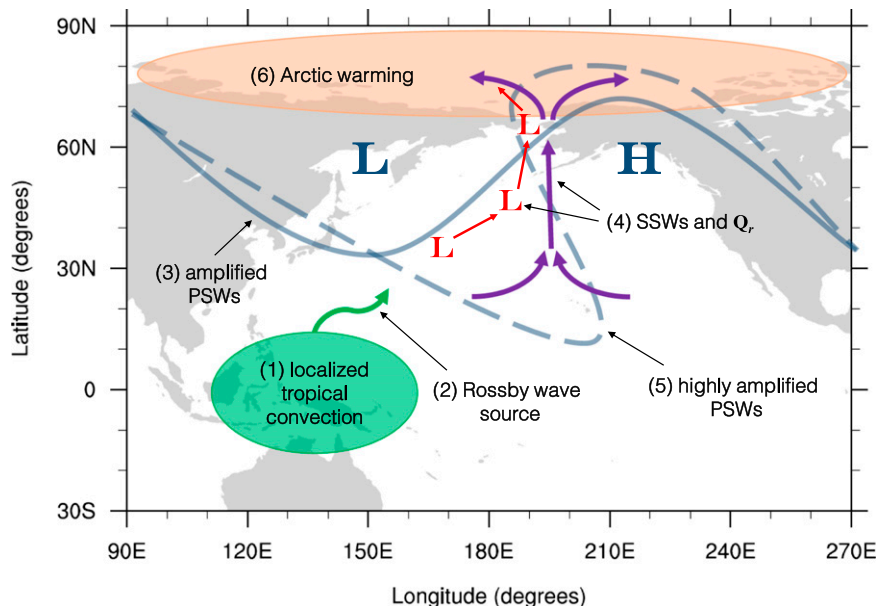


FIG. 11. Schematic presentation of the principal features that lead to Arctic warming during the PSW life cycle over the North Pacific. The features are numbered in chronological order and described in section 5.

Alaska retrogrades to the west, blocking any additional transport into the Arctic.

- 6) TCW values in the Arctic remain elevated following the peak of the PSW life cycle. This produces enhanced downward IR that leads to Arctic surface warming (BL15; Flounoy et al. 2016).

With respect to the idealized model, we found that it does not reproduce the SSW activity observed in reanalysis data during the PSW life cycle. The lack of SSW activity may partly be explained by the absence of diabatic heating through latent heat release that would otherwise amplify the SSWs (Lackmann 2002; Grams et al. 2011; Willison et al. 2013; Lin 2004). More importantly, the model has an insufficient spinup time for baroclinic instability to develop SSWs from a climatological initial state and for the resulting SSWs to interact with the forced PSWs. Nevertheless, the lack of SSW activity in the model is informative because it is highly suggestive of the importance of the SSWs in amplifying the PSWs, which further enhances the transport of heat and moisture to the highest latitudes—features that are observed in reanalysis data but not in the model.

For future work, it would be beneficial to initialize the model with daily fields rather than a climatological initial state or to employ a fully coupled global climate model. Presumably, the role of SSWs would be more prominent in such experiments. Also, it would be interesting to determine if the process described in Fig. 11 operates during different seasons, such as June–August, when the subtropical jet is less energized (a weaker Rossby wave source) and when low-frequency moisture transport into the Arctic primarily derives from continental source regions (Newman et al. 2012). Finally, high-resolution regional models could be employed to explore the sensitivity to topography of moisture transport into the Arctic. Moisture transport to the east or west of the Bering Strait may be reduced by precipitating parcels as they ascend over high topography.

Our study offers additional insight into the TEAM mechanism by revealing the important role that SSWs and ARs play in warming the Arctic during the PSW life cycle. Because the PSW life cycle can contribute to Arctic amplification independent of the flux–gradient relationship (BL15), we contend that the TEAM mechanism is a viable dynamical pathway, amongst others, to maintain a warmer Arctic in a warmer world (Budyko and Izrael 1991; Hoffert and Covey 1992; Miller et al. 2010; Lee 2014). However, it remains to be seen how much of the warming we have observed in the Arctic is due to the TEAM mechanism versus other processes and if the frequency of occurrence of the PSW life cycle is dominated by natural variability or by anthropogenic forcing—important questions that we plan to address in future work.

Acknowledgments. This study was supported by the National Science Foundation under Grants AGS-1139970, AGS-1401220, and AGS-1455577. Valuable comments from Michael Goss and George Sokolowsky helped to improve this manuscript. All coding was performed using the National Center for Atmospheric Research Command Language (NCL; NCAR Command Language 2015).

REFERENCES

- Abbot, D. S., and E. Tziperman, 2008: Sea ice, high-latitude convection, and equable climates. *Geophys. Res. Lett.*, **35**, L03702, doi:10.1029/2007GL032286.
- Aref, H., 1984: Stirring by chaotic advection. *J. Fluid Mech.*, **143**, 1–21, doi:10.1017/S0022112084001233.
- Baggett, C., and S. Lee, 2015: Arctic warming induced by tropically forced tapping of available potential energy and the role of the planetary-scale waves. *J. Atmos. Sci.*, **72**, 1562–1568, doi:10.1175/JAS-D-14-0334.1.
- Bao, J.-W., S. A. Michelson, P. J. Neiman, F. M. Ralph, and J. M. Wilczak, 2006: Interpretation of enhanced integrated water vapor bands associated with extratropical cyclones: Their formation and connection to tropical moisture. *Mon. Wea. Rev.*, **134**, 1063–1080, doi:10.1175/MWR3123.1.
- Barron, E. J., W. H. Peterson, D. Pollard, and S. L. Thompson, 1993: Past climate and the role of ocean heat transport: Model simulations for the Cretaceous. *Paleoceanography*, **8**, 785–798, doi:10.1029/93PA02227.
- Bolton, D., 1980: The computation of equivalent potential temperature. *Mon. Wea. Rev.*, **108**, 1046–1053, doi:10.1175/1520-0493(1980)108<1046:TCOEPT>2.0.CO;2.
- Budyko, M. I., and Y. A. Izrael, 1991: *Anthropogenic Climate Change*. University of Arizona Press, 485 pp.
- Cai, M., 2006: Dynamical greenhouse-plus feedback and polar warming amplification. Part I: A dry radiative–transportive climate model. *Climate Dyn.*, **26**, 661–675, doi:10.1007/s00382-005-0104-6.
- Carlson, T. N., 1980: Airflow through midlatitude cyclones and the comma cloud pattern. *Mon. Wea. Rev.*, **108**, 1498–1509, doi:10.1175/1520-0493(1980)108<1498:ATMCAT>2.0.CO;2.
- Dacre, H. F., P. A. Clark, O. Martinez-Alvarado, M. A. Stringer, and D. A. Lavers, 2015: How do atmospheric rivers form? *Bull. Amer. Meteor. Soc.*, **96**, 1243–1255, doi:10.1175/BAMS-D-14-00031.1.
- Dee, D. P., and Coauthors, 2011: The ERA-Interim reanalysis: Configuration and performance of the data assimilation system. *Quart. J. Roy. Meteor. Soc.*, **137**, 553–597, doi:10.1002/qj.828.
- De Vries, A. J., S. B. Feldstein, M. Riemer, E. Tyrlis, M. Sprenger, M. Baumgart, M. Fnais, and J. Lelieveld, 2016: Dynamics of tropical–extratropical interactions and extreme precipitation events in Saudi Arabia in autumn, winter and spring. *Quart. J. Roy. Meteor. Soc.*, **142**, 1862–1880, doi:10.1002/qj.2781.
- Ding, Q., J. M. Wallace, D. S. Battisti, E. J. Steig, A. J. E. Gallant, H.-J. Kim, and L. Geng, 2014: Tropical forcing of the recent rapid Arctic warming in northeastern Canada and Greenland. *Nature*, **509**, 209–212, doi:10.1038/nature13260.
- Doyle, J. G., G. Lesins, C. P. Thackray, C. Perro, G. J. Nott, T. J. Duck, R. Damoah, and J. R. Drummond, 2011: Water vapor intrusions into the High Arctic during winter. *Geophys. Res. Lett.*, **38**, L12806, doi:10.1029/2011GL047493.
- Draxler, R. R., and G. D. Rolph, 2015: HYSPPLIT—Hybrid Single Particle Lagrangian Integrated Trajectory Model. NOAA/Air

- Resources Laboratory, 31 August 2015. [Available online at <http://ready.arl.noaa.gov/HYSPLIT.php>.]
- Eckhardt, S., A. Stohl, H. Wernli, P. James, C. Forster, and N. Spichtinger, 2004: A 15-year climatology of warm conveyor belts. *J. Climate*, **17**, 218–237, doi:10.1175/1520-0442(2004)017<0218:AYCOWC>2.0.CO;2.
- ECMWF, 2009: The ERA-Interim project. European Centre for Medium-Range Weather Forecasts public datasets, accessed 25 October 2013. [Available online at <http://apps.ecmwf.int/datasets/data/interim-full-daily/levtype=sfc/>.]
- Farrell, B. F., 1990: Equable climate dynamics. *J. Atmos. Sci.*, **47**, 2986–2995, doi:10.1175/1520-0469(1990)047<2986:ECD>2.0.CO;2.
- Flournoy, M., S. B. Feldstein, and S. Lee, 2016: Exploring the tropically excited Arctic warming mechanism with BSRN station data: Links between tropical convection and Arctic downward infrared radiation. *J. Atmos. Sci.*, **73**, 1143–1158, doi:10.1175/JAS-D-14-0271.1.
- Francis, J. A., and S. J. Vavrus, 2012: Evidence linking Arctic amplification to extreme weather in mid-latitudes. *Geophys. Res. Lett.*, **39**, L06801, doi:10.1029/2012GL051000.
- Franzke, C., S. Lee, and S. B. Feldstein, 2004: Is the North Atlantic Oscillation a breaking wave? *J. Atmos. Sci.*, **61**, 145–160, doi:10.1175/1520-0469(2004)061<0145:ITNAOA>2.0.CO;2.
- , S. B. Feldstein, and S. Lee, 2011: Synoptic analysis of the Pacific–North American teleconnection pattern. *Quart. J. Roy. Meteor. Soc.*, **137**, 329–346, doi:10.1002/qj.768.
- Jimeno, L., M. Vázquez, R. Nieto, and R. M. Trigo, 2015: Atmospheric moisture transport, the bridge between ocean evaporation and Arctic ice melting. *Earth Syst. Dyn.*, **6**, 583–589, doi:10.5194/esd-6-583-2015.
- Grams, C. M., and Coauthors, 2011: The key role of diabatic processes in modifying the upper-tropospheric wave guide: A North Atlantic case-study. *Quart. J. Roy. Meteor. Soc.*, **137**, 2174–2193, doi:10.1002/qj.891.
- Guan, B., and D. E. Waliser, 2015: Detection of atmospheric rivers: Evaluation and application of an algorithm for global studies. *J. Geophys. Res. Atmos.*, **120**, 12 514–12 535, doi:10.1002/2015JD024257.
- Held, I. M., and M. J. Suarez, 1994: A proposal for the intercomparison of the dynamical cores of atmospheric general circulation models. *Bull. Amer. Meteor. Soc.*, **75**, 1825–1830, doi:10.1175/1520-0477(1994)075<1825:APFTIO>2.0.CO;2.
- Henderson, S. A., E. D. Maloney, and E. A. Barnes, 2016: The influence of the Madden–Julian oscillation on Northern Hemisphere winter blocking. *J. Climate*, **29**, 4597–4616, doi:10.1175/JCLI-D-15-0502.1.
- Higgins, R. W., J.-K. E. Schemm, W. Shi, and A. Leetmaa, 2000: Extreme precipitation events in the western United States related to tropical forcing. *J. Climate*, **13**, 793–820, doi:10.1175/1520-0442(2000)013<0793:EPEITW>2.0.CO;2.
- Hoffert, M. I., and C. Covey, 1992: Deriving global climate sensitivity from paleoclimate reconstructions. *Nature*, **360**, 573–576, doi:10.1038/360573a0.
- Honda, M., J. Inoue, and S. Yamane, 2009: Influence of low Arctic sea-ice minima on anomalously cold Eurasian winters. *Geophys. Res. Lett.*, **36**, L08707, doi:10.1029/2008GL037079.
- Hoskins, B. J., and D. J. Karoly, 1981: The steady linear response of a spherical atmosphere to thermal and orographic forcing. *J. Atmos. Sci.*, **38**, 1179–1196, doi:10.1175/1520-0469(1981)038<1179:TSLROA>2.0.CO;2.
- , M. E. McIntyre, and A. W. Robertson, 1985: On the use and significance of isentropic potential vorticity maps. *Quart. J. Roy. Meteor. Soc.*, **111**, 877–946, doi:10.1002/qj.49711147002.
- Jin, F., and B. J. Hoskins, 1995: The direct response to tropical heating in a baroclinic atmosphere. *J. Atmos. Sci.*, **52**, 307–319, doi:10.1175/1520-0469(1995)052<0307:TDRTH>2.0.CO;2.
- Kalnay, E., and Coauthors, 1996: The NCEP/NCAR 40-Year Reanalysis Project. *Bull. Amer. Meteor. Soc.*, **77**, 437–471, doi:10.1175/1520-0477(1996)077<0437:TNYRP>2.0.CO;2.
- Kapsch, M.-L., R. G. Graversen, and M. Tjernström, 2013: Springtime atmospheric energy transport and the control of Arctic summer sea-ice extent. *Nat. Climate Change*, **3**, 744–748, doi:10.1038/nclimate1884.
- Kiladis, G. N., and S. B. Feldstein, 1994: Rossby wave propagation into the tropics in two GFDL general circulation models. *Climate Dyn.*, **9**, 245–252, doi:10.1007/BF00208256.
- Knippertz, P., 2007: Tropical–extratropical interactions related to upper-level troughs at low latitudes. *Dyn. Atmos. Oceans*, **43**, 36–62, doi:10.1016/j.dynatmoce.2006.06.003.
- , and H. Wernli, 2010: A Lagrangian climatology of tropical moisture exports to the Northern Hemispheric extratropics. *J. Climate*, **23**, 987–1003, doi:10.1175/2009JCLI3333.1.
- , —, and G. Gläser, 2013: A global climatology of tropical moisture exports. *J. Climate*, **26**, 3031–3045, doi:10.1175/JCLI-D-12-00401.1.
- Krichak, S. O., J. Barkan, J. S. Breitgand, S. Gualdi, and S. B. Feldstein, 2015: The role of the export of tropical moisture into midlatitudes for extreme precipitation events in the Mediterranean region. *Theor. Appl. Climatol.*, **121**, 499–515, doi:10.1007/s00704-014-1244-6.
- Kump, L. R., and D. Pollard, 2008: Amplification of Cretaceous warmth by biological cloud feedbacks. *Science*, **320**, 195, doi:10.1126/science.1153883.
- Lackmann, G. M., 2002: Cold-frontal potential vorticity maxima, the low-level jet, and moisture transport in extratropical cyclones. *Mon. Wea. Rev.*, **130**, 59–74, doi:10.1175/1520-0493(2002)130<0059:CFPVMT>2.0.CO;2.
- Langen, P. L., and V. A. Alexeev, 2007: Polar amplification as a preferred response in an idealized aquaplanet GCM. *Climate Dyn.*, **29**, 305–317, doi:10.1007/s00382-006-0221-x.
- Lee, S., 2012: Testing of the tropically excited Arctic warming mechanism (TEAM) with traditional El Niño and La Niña. *J. Climate*, **25**, 4015–4022, doi:10.1175/JCLI-D-12-00055.1.
- , 2014: A theory for polar amplification from a general circulation perspective. *Asia-Pac. J. Atmos. Sci.*, **50**, 31–43, doi:10.1007/s13143-014-0024-7.
- , and C. Yoo, 2014: On the causal relationship between poleward heat flux and the equator-to-pole temperature gradient: A cautionary tale. *J. Climate*, **27**, 6519–6525, doi:10.1175/JCLI-D-14-00236.1.
- , S. B. Feldstein, D. Pollard, and T. S. White, 2011a: Do planetary wave dynamics contribute to equable climates? *J. Climate*, **24**, 2391–2404, doi:10.1175/2011JCLI3825.1.
- , T. Gong, N. Johnson, S. B. Feldstein, and D. Pollard, 2011b: On the possible link between tropical convection and the Northern Hemisphere Arctic surface air temperature change between 1958 and 2001. *J. Climate*, **24**, 4350–4367, doi:10.1175/2011JCLI4003.1.
- Lin, S. J., 2004: A “vertically Lagrangian” finite-volume dynamical core for global models. *Mon. Wea. Rev.*, **132**, 2293–2307, doi:10.1175/1520-0493(2004)132<2293:AVLFDG>2.0.CO;2.
- Liu, C., and E. A. Barnes, 2015: Extreme moisture transport into the Arctic linked to Rossby wave breaking. *J. Geophys. Res. Atmos.*, **120**, 3774–3788, doi:10.1002/2014JD022796.
- Liu, J., J. A. Curry, H. Wang, M. Song, and R. M. Horton, 2012: Impact of declining Arctic sea ice on winter snowfall. *Proc.*

- Natl. Acad. Sci. USA*, **109**, 4074–4079, doi:[10.1073/pnas.1114910109](https://doi.org/10.1073/pnas.1114910109).
- Miller, G. H., R. B. Alley, J. Brigham-Grette, J. J. Fitzpatrick, L. Polyak, M. C. Serreze, and J. W. C. White, 2010: Arctic amplification: Can the past constrain the future? *Quat. Sci. Rev.*, **29**, 1779–1790, doi:[10.1016/j.quascirev.2010.02.008](https://doi.org/10.1016/j.quascirev.2010.02.008).
- Moore, B. J., P. J. Neiman, F. M. Ralph, and F. E. Barthold, 2012: Physical processes associated with heavy flooding rainfall in Nashville, Tennessee, and vicinity during 1–2 May 2010: The role of an atmospheric river and mesoscale convective systems. *Mon. Wea. Rev.*, **140**, 358–378, doi:[10.1175/MWR-D-11-00126.1](https://doi.org/10.1175/MWR-D-11-00126.1).
- Mundhenk, B., E. A. Barnes, and E. Maloney, 2016: All-season climatology and variability of atmospheric river frequencies over the North Pacific. *J. Climate*, **29**, 4885–4903, doi:[10.1175/JCLI-D-15-0655.1](https://doi.org/10.1175/JCLI-D-15-0655.1).
- NCAR Command Language, 2015: NCL version 6.3.0. UCAR/NCAR—Computational and Information Systems Laboratory. [Available online at <http://www.ncl.ucar.edu/Download/>.]
- Neff, W., G. P. Compo, F. M. Ralph, and M. D. Shupe, 2014: Continental heat anomalies and the extreme melting of the Greenland ice surface in 2012 and 1889. *J. Geophys. Res. Atmos.*, **119**, 6520–6536, doi:[10.1002/2014JD021470](https://doi.org/10.1002/2014JD021470).
- Neiman, P. J., F. M. Ralph, G. A. Wick, J. Lundquist, and M. D. Dettinger, 2008: Meteorological characteristics and overland precipitation impacts of atmospheric rivers affecting the west coast of North America based on eight years of SSM/I satellite observations. *J. Hydrometeorol.*, **9**, 22–47, doi:[10.1175/2007JHM855.1](https://doi.org/10.1175/2007JHM855.1).
- , L. J. Schick, F. M. Ralph, M. Hughes, and G. A. Wick, 2011: Flooding in western Washington: The connection to atmospheric rivers. *J. Hydrometeorol.*, **12**, 1337–1358, doi:[10.1175/2011JHM1358.1](https://doi.org/10.1175/2011JHM1358.1).
- Newell, R. E., N. E. Newell, Y. Zhu, and C. Scott, 1992: Tropospheric rivers?—A pilot study. *Geophys. Res. Lett.*, **19**, 2401–2404, doi:[10.1029/92GL02916](https://doi.org/10.1029/92GL02916).
- Newman, M., G. N. Kiladis, K. M. Weickmann, F. M. Ralph, and P. D. Sardeshmukh, 2012: Relative contributions of synoptic and low-frequency eddies to time-mean atmospheric moisture transport, including the role of atmospheric rivers. *J. Climate*, **25**, 7341–7361, doi:[10.1175/JCLI-D-11-00665.1](https://doi.org/10.1175/JCLI-D-11-00665.1).
- Ottino, J., 1990: Mixing, chaotic advection, and turbulence. *Annu. Rev. Fluid Mech.*, **22**, 207–253, doi:[10.1146/annurev.fl.22.010190.001231](https://doi.org/10.1146/annurev.fl.22.010190.001231).
- Overland, J. E., and M. Wang, 2010: Large-scale atmospheric circulation changes are associated with the recent loss of Arctic sea ice. *Tellus*, **62A**, 1–9, doi:[10.1111/j.1600-0870.2009.00421.x](https://doi.org/10.1111/j.1600-0870.2009.00421.x).
- Ralph, F. M., and M. D. Dettinger, 2011: Storms, floods and the science of atmospheric rivers. *Eos, Trans. Amer. Geophys. Union*, **92**, 265–272, doi:[10.1029/2011EO320001](https://doi.org/10.1029/2011EO320001).
- , P. J. Neiman, and G. A. Wick, 2004: Satellite and CALJET aircraft observations of atmospheric rivers over the eastern North Pacific Ocean during the winter of 1997/98. *Mon. Wea. Rev.*, **132**, 1721–1745, doi:[10.1175/1520-0493\(2004\)132<1721:SACAOO>2.0.CO;2](https://doi.org/10.1175/1520-0493(2004)132<1721:SACAOO>2.0.CO;2).
- , —, G. N. Kiladis, K. Weickmann, and D. W. Reynolds, 2011: A multiscale observational case study of a Pacific atmospheric river exhibiting tropical–extratropical connections and a mesoscale frontal wave. *Mon. Wea. Rev.*, **139**, 1169–1189, doi:[10.1175/2010MWR3596.1](https://doi.org/10.1175/2010MWR3596.1).
- Roberge, A., J. R. Gyakum, and E. H. Atallah, 2009: Analysis of intense poleward water vapor transports into high latitudes of western North America. *Wea. Forecasting*, **24**, 1732–1747, doi:[10.1175/2009WAF2222198.1](https://doi.org/10.1175/2009WAF2222198.1).
- Sardeshmukh, P. D., and B. J. Hoskins, 1988: The generation of global rotational flow by steady idealized tropical divergence. *J. Atmos. Sci.*, **45**, 1228–1250, doi:[10.1175/1520-0469\(1988\)045<1228:TGOGRF>2.0.CO;2](https://doi.org/10.1175/1520-0469(1988)045<1228:TGOGRF>2.0.CO;2).
- Serreze, M. C., and R. G. Barry, 2011: Processes and impacts of Arctic amplification: A research synthesis. *Global Planet. Change*, **77**, 85–96, doi:[10.1016/j.gloplacha.2011.03.004](https://doi.org/10.1016/j.gloplacha.2011.03.004).
- Smith, B. L., S. E. Yuter, P. J. Neiman, and D. E. Kingsmill, 2010: Water vapor fluxes and orographic precipitation over Northern California associated with a landfalling atmospheric river. *Mon. Wea. Rev.*, **138**, 74–100, doi:[10.1175/2009MWR2939.1](https://doi.org/10.1175/2009MWR2939.1).
- Sodemann, H., and A. Stohl, 2013: Moisture origin and meridional transport in atmospheric rivers and their association with multiple cyclones. *Mon. Wea. Rev.*, **141**, 2850–2868, doi:[10.1175/MWR-D-12-00256.1](https://doi.org/10.1175/MWR-D-12-00256.1).
- Sriver, R. L., and M. Huber, 2007: Observational evidence for an ocean heat pump induced by tropical cyclones. *Nature*, **447**, 577–580, doi:[10.1038/nature05785](https://doi.org/10.1038/nature05785).
- Stohl, A., and P. James, 2004: A Lagrangian analysis of the atmospheric branch of the global water cycle. Part I: Method description, validation, and demonstration for the August 2002 flooding in central Europe. *J. Hydrometeorol.*, **5**, 656–678, doi:[10.1175/1525-7541\(2004\)005<0656:ALAOTA>2.0.CO;2](https://doi.org/10.1175/1525-7541(2004)005<0656:ALAOTA>2.0.CO;2).
- Thorncroft, C. D., B. J. Hoskins, and M. E. McIntyre, 1993: Two paradigms of baroclinic-wave life-cycle behaviour. *Quart. J. Roy. Meteor. Soc.*, **119**, 17–55, doi:[10.1002/qj.49711950903](https://doi.org/10.1002/qj.49711950903).
- Walsh, J. E., W. L. Chapman, V. Romanovsky, J. H. Christensen, and M. Stendel, 2008: Global climate model performance over Alaska and Greenland. *J. Climate*, **21**, 6156–6174, doi:[10.1175/2008JCLI2163.1](https://doi.org/10.1175/2008JCLI2163.1).
- Willison, J., W. A. Robinson, and G. M. Lackmann, 2013: The importance of resolving mesoscale latent heating in the North Atlantic storm track. *J. Atmos. Sci.*, **70**, 2234–2250, doi:[10.1175/JAS-D-12-0226.1](https://doi.org/10.1175/JAS-D-12-0226.1).
- Winton, M., 2006: Amplified Arctic climate change: What does surface albedo feedback have to do with it? *Geophys. Res. Lett.*, **33**, L03701, doi:[10.1029/2005GL025244](https://doi.org/10.1029/2005GL025244).
- Woods, C., R. Caballero, and G. Svensson, 2013: Large-scale circulation associated with moisture intrusions into the Arctic during winter. *Geophys. Res. Lett.*, **40**, 4717–4721, doi:[10.1002/grl.50912](https://doi.org/10.1002/grl.50912).
- Yoo, C., S. B. Feldstein, and S. Lee, 2011: The impact of the Madden–Julian Oscillation trend on the Arctic amplification of surface air temperature during the 1979–2008 boreal winter. *Geophys. Res. Lett.*, **38**, L24804, doi:[10.1029/2011GL049881](https://doi.org/10.1029/2011GL049881).
- , S. Lee, and S. B. Feldstein, 2012a: Arctic response to an MJO-like tropical heating in an idealized GCM. *J. Atmos. Sci.*, **69**, 2379–2393, doi:[10.1175/JAS-D-11-0261.1](https://doi.org/10.1175/JAS-D-11-0261.1).
- , —, and —, 2012b: Mechanisms of extratropical surface air temperature change in response to the Madden–Julian oscillation. *J. Climate*, **25**, 5777–5790, doi:[10.1175/JCLI-D-11-00566.1](https://doi.org/10.1175/JCLI-D-11-00566.1).
- Zhu, Y., and R. E. Newell, 1998: A proposed algorithm for moisture fluxes from atmospheric rivers. *Mon. Wea. Rev.*, **126**, 725–735, doi:[10.1175/1520-0493\(1998\)126<0725:APAFMF>2.0.CO;2](https://doi.org/10.1175/1520-0493(1998)126<0725:APAFMF>2.0.CO;2).